Applied Catalysis B: Environmental 142–143 (2013) 718–728

Contents lists available at SciVerse ScienceDirect

Applied Catalysis B: Environmental

journal homepage: www.elsevier.com/locate/apcatb

Novel visible light active graphitic C_3N_4–TiO_2 composite photocatalyst: Synergistic synthesis, growth and photocatalytic treatment of hazardous pollutants

Kishore Sridharan, Eunyong Jang, Tae Joo Park*

Department of Materials Engineering, Hanyang University, Ansan 426 791, Republic of Korea

ARTICLE INFO

Article history:
Received 28 March 2013
Received in revised form 30 May 2013
Accepted 31 May 2013
Available online 12 June 2013

Keywords:
Graphitic carbon nitride
TiO_2
Visible light active photocatalyst
Methylene Blue
Cr(VI) reduction

ABSTRACT

Novel visible light active graphitic carbon nitride TiO_2 (g-C_3N_4–TiO_2) composite photocatalyst is prepared through a thermal transformation methodology. C and N co-doped TiO_2 (TGU) microspherical nanorods, were prepared initially by hydrothermal process, using urea and D-glucose as the dopant precursors. Pyrolysis of TGU at 300 °C in open air, transformed it to g-C_3N_4–TiO_2 (TCN) composite. Structural and morphological characterization on TCN composites, using X-ray diffraction (XRD), energy dispersive X-ray spectroscopy (EDS) and transmission electron microscopy (TEM), reveals the growth of g-C_3N_4 (CN nanosheets) on doped TiO_2. Plausible growth mechanism is predicted based on the morphological investigations. Band gap energy of the samples was estimated using UV–vis diffuse reflectance (DRS) spectroscopy and TCN composites were found to be active under visible light. Efficiency of the prepared samples were investigated by monitoring the degradation of Methylene Blue (MB) and by the reduction of Cr(VI) ions. Improved photocatalytic activity in TCN is observed owing to the formation of a synergistic heterojunction, which facilitates a fast electron transfer at the interface between CN and doped TiO_2. Visible light absorption capability of both CN and doped TiO_2, complements the synergy factor. This synergistic approach, could prove useful for the design and development of other visible light active photocatalysts with high chemical stability.

1. Introduction

Multi-dimensional nanostructures of metals and semiconductors have always attracted material research scientists due to their extensive applications in the field of catalysis, sensing, hydrogen generation, optics, and optoelectronics [1–6] etc. Titanium dioxide (TiO_2) is one special oxide semiconductor that has been vastly studied, owing to its multifunctionality. Photocatalysis, dye sensitized solar cells (DSSCs), hydrogen energy production by light water splitting [7–14] etc., are some of the important fields in which TiO_2 plays a major role. Even though TiO_2 is sensitive only to UV light due to its large band gap (~3.0 and ~3.2 eV for rutile and anatase, respectively), still is preferred as an ideal candidate to be developed as a visible light active photocatalyst because of its high chemical stability, environmental friendliness and low synthesis cost. Development of visible light active TiO_2 has been a major research topic in the past decade and still continues to be an important one. The advancements in the field of visible light active TiO_2, prepared by incorporating various materials such as metals, non-metals and rare earth metals, have been briefly summarized in many review articles [15–21].

Carbon nitrides have been identified as a new form of organic polymer-like material with diverse properties [22]. Graphitic carbon nitride (g-C_3N_4, referred hereafter as CN) is regarded as the most stable allotrope of carbon nitride, that has been prepared through various techniques [23] and is proving to be a potentially viable candidate for various applications. Goettmann et al., employed it as a metal-free catalyst for Friedel-Crafts reaction of benzene [24], for the activation of CO_2 [25] and for the cyclization of functional nitriles and alkynes [26]. Yang et al. [27] synthesized pristine nitrogen-rich CN through a low temperature condensation technique and investigated its hydrogen storage behavior. The energy band-gap of CN was estimated to ~2.7 eV by Wang et al. [28], who reported its potential for the production of H_2 under visible light irradiation. Since then many research groups started investigating the use of CN by different methods for environmental remediation and for H_2 production owing to its environmental friendliness and the abundant availability of its precursors. Recently, urea was introduced as the cheapest source for producing CN nanosheets. Zou et al. [29] converted urea into CN through pyrolysis, using mesoporous TiO_2 as a hard template and Liu et al. [30] prepared CN without the assistance of

* Corresponding author. Tel.: +82 31 400 5223; fax: +82 31 436 8146.
E-mail address: tjp@hanyang.ac.kr (T.J. Park).

0926-3373/$ – see front matter © 2013 Elsevier B.V. All rights reserved.
http://dx.doi.org/10.1016/j.apcatb.2013.05.077

any template by pyrolysis of urea under ambient conditions. High recombination rate of electron–hole ($e^- - h^+$) pair in CN, is one of the major concerns limiting its photocatalytic efficiency. Doping and coupling are the two methods introduced for lowering the recombination rate. (1) Doping: CN has been doped with metals such as Au [31], Ag [32], Fe [33] and non-metals such as P [34], B [35], S [36]. (2) Organic–inorganic coupling process: Inorganic materials such as MWCNT [37], Graphene [38], Bi_2WO_6 [39], TaON [40], AgBr/I [41], $SmVO_4$ [42], Fe_3O_4 [43] have been coupled with CN to improve its visible light photocatalytic activity.

Till date, not many reports are available on the synthesis and visible light photocatalytic activity studies on g-C_3N_4–TiO_2 (referred hereafter as TCN) composites. Yan and Yang [44], reported the visible light H_2 evolution using TCN composites prepared through ball milling technique. Zou et al. [29] prepared g-C_3N_4 by heating urea in the presence of mesoporous TiO_2 spheres, after which TiO_2 was removed by etching using Hydrofluoric acid (HF). We here report a novel methodology to prepare TCN composite photocatalyst through a simple strategy. Microspheres of C and N codoped TiO_2 with stacked nanorods (referred hereafter as TGU) were initially prepared through a hydrothermal process with D-glucose and urea as the carbon and nitrogen source. Pyrolysis of TGU in air at 300 and 500 °C, resulted in color change, from brown to orange-tan and yellow, respectively. TEM investigations revealed the presence of two dimensional CN nanosheets with TiO_2 particles stacked/intercalated in between them, forming TCN composite. The strong bonding formed during the hydrothermal growth of TGU develops a synergy between TiO_2 and CN during the thermal formation of TCN, is the main advantage of our synthetic approach. Motivation for the use of TiO_2 as the inorganic coupler are due to the following reasons: (i) TiO_2 is cheap, environmental friendly and chemically stable as like CN and hence their combination can offer excellent chemical stability, (ii) in TiO_2 P25 (Degussa, with 80% Anatase and 20% Rutile) the rutile phase acts as an electron sink, decreasing the recombination rate of $e^- - h^+$ pair [45]. A similar phenomenon is expected in the TCN composite too. (iii) To the best of our knowledge there are no reports till date on the use of doped TiO_2 coupled with organic CN nanosheets in the photocatalytic reduction of Cr(VI) ions. The synergy formed between C–N codoped TiO_2 with CN nanosheets is believed to enhance the oxidative power of photoinduced holes in the valance band (VB), proves useful for the reduction of toxic metal ions such as Cr(VI). Photocatalytic efficiency of the prepared photocatalysts were determined by studying the degradation of Methylene Blue (MB) dye and by Cr(VI) reduction under visible light irradiation. For a comparison the photocatalytic activity of P25 TiO_2 (Degussa) were also investigated under the same experimental conditions.

2. Experimental details

2.1. Materials

Titanium tetraisopropoxide ($C_{12}H_{28}O_4Ti$, TTIP), hydrochloric acid (HCl, 20%) cetyltrimethylammonium bromide ($C_{19}H_{42}BrN$, CTAB), urea (CH_4N_2O) and Methylene Blue ($C_{16}H_{24}ClN_3O_3S{\cdot}3H_2O$, MB) dye were purchased from Dae-Jung Chemicals, Korea. D-Glucose ($C_6H_{12}O_6$) and Potassium Dichromate ($K_2Cr_2O_7$) were purchased from Sigma Aldrich and Junsei Chemicals, Korea respectively. The precursors were used as received without purifying further. Deionized water was used throughout the experiments.

2.2. Preparation of photocatalysts

In a 5 mM solution of CTAB, 0.01 M of D-glucose and urea, respectively were dissolved under magnetic stirring. The above solution was transferred to a solution containing 1 ml of TTIP dissolved in 30 ml of HCl under magnetic stirring. This final solution was transferred into a Teflon-lined stainless steel autoclave of 100 ml capacity. The sealed autoclave was placed in an electric oven and the hydrothermal reaction was carried out at 150 °C for 12 h. After the autoclave was cooled down naturally, the sediments were separated through natural sedimentation and centrifugation. The centrifuged sediments were dried in an oven at 100 °C for 12 h and the sample was named as TGU. TGU taken in an uncovered crucible, was thermally treated for 2 h in open air inside a muffle furnace. The product obtained by the thermal treatment of TGU at 300 and 500 °C was named as TCN300 and TCN500, respectively.

2.3. Characterization

Powder X-ray diffraction (XRD) patterns of the prepared samples were obtained using an X-ray diffractometer (*Rigaku-Dmax 2500*) with Cu-Kα radiation (λ = 0.15405 nm, 40 kV, 100 mA). The samples were scanned in the range $2\theta = 20–80^\circ$. The morphology of the prepared samples was analyzed using a *MIRA3 TESCAN* high resolution scanning electron microscope (SEM), equipped with a high brightness Schottky field emission gun. The surface area and porosity of the samples were estimated by measuring the nitrogen adsorption–desorption isotherms on a *Micrometrics ASAP 2010* system. Photoluminescence (PL) spectra of the samples were measured at room temperature on a *Fluorolog®* – 3 Spectrofluorometer (*Horiba Jobin Yvon*) system, consisting of a cw 450 W Xenon short arc excitation source. Samples for PL measurements were prepared by dissolving the powder sample in ethanol, with constant concentration. High-resolution transmission electron microscopy (HRTEM), EDS and selected area electron diffraction pattern (SAED), were performed on a *JEOL 2010F FE-TEM* operating at 200 kV. The samples for TEM were prepared by dropping the sample solution, dissolved in ethanol onto a carbon-coated copper grid. UV–vis diffuse reflectance spectra (DRS), of the photocatalysts were recorded on a *JASCO V-550* UV-visible spectrophotometer equipped with an integrating sphere (*JASCO ISV-469*), using a dedicated powder sample holder (*JASCO PSH-001*).

2.4. Visible light photocatalytic activity studies

The photocatalytic activity of the prepared photocatalysts was assessed by observing the degradation of MB dye under visible light (λ > 400 nm) irradiation. Home-made irradiation system was constructed using a 100 W Halogen lamp (*HI-Spot 95*), purchased from *Osram Sylvania Inc.*, with UV-stop feature. Reaction slurry was prepared in a crystallizing dish (*Duran®*) of 300 ml capacity by suspending 25 mg of photocatalyst in 200 ml of MB dye solution (concentration: 1.5×10^{-5} M). The body of the dish containing the slurry was covered using aluminum foil and was stirred under dark for 1 h, to ensure the adsorption of MB dye on the surface of the photocatalyst. The Halogen lamp was placed 6 cm above the dish containing the slurry which was agitated at 200 rpm. Aliquots were collected at regular intervals of time until the MB dye degraded, and their UV–vis absorption spectra were recorded using a *JASCO V-550* spectrometer, from which the degradation efficiency of the photocatalyst was calculated.

Reaction slurry for the photocatalytic reduction of hexavalent chromium was prepared in a 300 ml crystallizing dish by suspending 50 mg of photocatalyst in 200 ml of 10 ppm Cr(VI) solution ($K_2Cr_2O_7$). The slurry had a pH of 5 and was left unaltered. All other photocatalytic experimental conditions for Cr(VI) reduction remained the same, as described above (MB dye degradation experiment). The aliquots collected were filtered using a filter paper and the Cr(VI) reduction efficiency of the photocatalysts were determined by analyzing their UV–vis absorption spectra.

3. Results and discussion

The physical appearance of TGU sample and its corresponding XRD pattern is shown in Fig. 1a and b, respectively. The observed peaks of all TGU samples can be indexed to the pure tetragonal rutile phase of TiO_2 (JCPDS card no # 21-1276) with lattice constants $a = 4.593$ Å and $c = 2.985$ Å. The XRD pattern of P25 (pure TiO_2) is also included for the sake of comparison.

3.1. Growth of C and N codoped TiO_2 microspheres stacked with nanorods (TGU)

Liu et al. [46] reported the directed growth of TiO_2 nanorods into microspheres under hydrothermal conditions using urea. TiO_2 nuclei were found to be actively linked to the coordination sites in the presence of the surfactant, where the nanorods grew in the form of 3D microspheres, through Ostwald ripening process. Surfactant-less synthesis did not result in the formation of microspheres. Similarly, another study reported the acid–base catalysis of titanium sulfate using urea for the formation of TiO_2 microspheres [47]. H_2SO_4 was used as the acid catalyst to suppress nucleation. Urea, used as the base catalyst, underwent thermal decomposition under hydrothermal conditions. Nucleation rate increased and the electrostatic repulsion between primary nanoparticles were weak, when the pH of the solution approached isoelectric point pH of TiO_2 [48]. Initiation of condensation reaction, promoted interparticle agglomeration and organized the spherical aggregates into chain-like assemblies to form microspheres.

In our case, the growth mechanism is a combination of the above mentioned mechanisms and is depicted in Scheme 1 (step 1). HCl acts the acid catalyst, controls the hydrolysis and suppresses nucleation. CTAB as the surfactant, influences TiO_2 nuclei to be linked to the coordination sites and under hydrothermal conditions and urea, catalyzes the nucleation and formation of nanorods [Eqs. (1) and (2)]. The following reactions of the precursors could take place under hydrothermal conditions.

$$NH_2CONH_2 + 3H_2O \rightarrow 2NH_3{\cdot}H_2O + CO_2 \quad (1)$$

$$2NH_3{\cdot}H_2O + CO_2 \rightarrow 2NH_4^+ + CO_3^{2-} \quad (2)$$

$$C_6H_{12}O_6 + C_6H_4O_2 \rightarrow 4H_2O \quad (3)$$

$$C_{12}H_{28}O_4Ti + 2H_2O \rightarrow TiO_2 + 4C_3H_7OH \quad (4)$$

Condensation reaction is initiated, when the pH of the solution reaches the isoelectric point of TiO_2. CTAB molecules link the spherical chain-like assemblies of TiO_2 to the coordination site from where the growth of nanorods takes place. On the other hand, Dong et al. [49] reported the hydrothermal preparation (160 °C for 12 h) of C-doped TiO_2 by employing D-glucose as the carbon precursor. Under hydrothermal conditions, it could be speculated that polymerization of D-glucose is catalyzed by the presence of Ti molecules during hydrolysis [50]. D-Glucose then carbonizes into hydrophillic carbon colloid [49,51,52] and forms O—Ti—C bond by long term interaction with Ti molecules. Therefore, the addition of urea and D-glucose results in the formation of C and N codoped TiO_2 (TGU) microspheres with stacked nanorods. Fig. 1c–f shows the SEM images under different magnifications of the hydrothermally synthesized TGU samples. Fig. 1f is the magnified image obtained from the rectangular area marked in Fig. 1e, which shows that nanorods are assembled in the form of microspheres. EDS and corresponding elemental maps obtained on TGU is shown in Fig. S1 (Supplementary content). The large cauliflower shape of TGU particle with stacked nanorods is schematically represented in step 1 of Scheme 1 (magnified image).

3.2. Growth of TCN from TGU

Scheme 1 (step 2) shows the growth of TCN from TGU during calcination. The hydrothermal product obtained after drying could possibly contain isocyanic acid adsorbed on the surface of TiO_2, as a residue. Moreover, the hydroxyl ions (OH) present on the surface of TiO_2 during the carbonization reaction of D-glucose are nucleophilic, and form $Ti—NH_2$ and CO_2, during its reaction with isocyanic acid [Eq. (5)] [29,53]. Cyanamide is formed by further reaction [Eq. (6)] and it polymerizes to yield g-C_3N_4–TiO_2 (TCN) composites [Eq. (7)].

$$Ti—OH + O{=}C{=}NH \rightarrow Ti—NH_2 + CO_2 \quad (5)$$

$$Ti—NH_2 + HO—C{\equiv}N \rightarrow Ti—OH + H_2N—C{\equiv}N \quad (6)$$

$$Ti—OH + 3H_2N—C{\equiv}N \rightarrow C_3N_4—TiO_2 + 2NH_3 \quad (7)$$

The photograph of the orange-tan colored powder is shown in Fig. 2a, depicts the physical appearance of TCN300 photocatalyst and Fig. 2b shows its corresponding XRD pattern. The XRD peaks of TCN300 correspond to pure rutile phase of TiO_2. The peak formed at $2\theta = 27.4°$ matches both the (1 1 0) plane of rutile TiO_2 and the (0 0 2) plane of g-C_3N_4. TCN300 sample was etched using HF solution [29] to yield CN nanosheets and its corresponding XRD pattern (Fig. 2b) shows the same peak at $2\theta = 27.4°$, which is consistent with previous reports [41,42]. The existence of CN nanosheets was further confirmed by TEM imaging and EDS.

Fig. 2c and d (magnified from the area marked in Fig. 2c) shows the SEM images of the TCN300. The stacked nanorods, as seen in TGU sample (Fig. 1e), were found to be broken down owing to the thermal treatment (300 °C), which results in the two dimensional sheets of g-C_3N_4, with small TiO_2 particles intercalated between the layers of the nanosheets as shown in TEM image of TCN300 sample (Fig. 2e). The magnified TEM image and SAED (spot diffraction) pattern of the nanoparticle, from the red encircled area marked in Fig. 2e (Fig. S2a, Supplementary Content) and its corresponding lattice resolved HRTEM image in Fig. S2b (Supplementary Content) confirm the single crystalline nature of the particles. EDS spectra in Fig. 2f, shows the presence of elements C, N, Ti, and O. Their weight and atomic percentages are shown in the table given as the inset of Fig. 2f.

The physical appearance and XRD pattern of TCN500 photocatalyst sample are shown in Fig. 3a and b, respectively. Like TGU and TCN300, the XRD pattern of TCN500, can also be indexed to pure rutile phase of TiO_2. SEM images in Fig. 3c and d indicate the presence of clustered nanoparticles which were confirmed using TEM as shown in Fig. S3 (Supplementary Content). Unlike TCN300, the formation of CN nanosheets in TCN500 sample was poor as seen from TEM image of Fig. 3e. EDS data (inset of Figs. 2f and 3f) shows that the weight ratio of N in TCN500 is much lower than that in TCN300, which can be considered as an evidence for the poor formation of CN. But the weight ratio of C is still considerably high, because of the carbonization of D-glucose, which increases the overall C content. Poor formation of CN in TCN500, is because of the open air pyrolysis of TGU at high temperature (500 °C). Liu et al. [30] reported that the pyrolysis-generated gas phase intermediates of urea leave the system when it is pyrolyzed in an open crucible at high temperatures, which hardly yields CN nanosheets. It is well known that the ammonia (NH_3) gas formed during the pyrolysis of urea at a temperature below 200 °C is well adsorbed on the surface of TGU during the hydrothermal synthesis. Therefore, the loss of gases is minimum during the formation of TCN300, and the as formed CN nanosheets are attached synergistically to the doped TiO_2 particles by covalent bonding [54]. A heterojunction is formed between g-C_3N_4 and doped TiO_2, can be called as a "synergistic heterojunction". On the other hand, at high temperatures (500 °C), the loss of

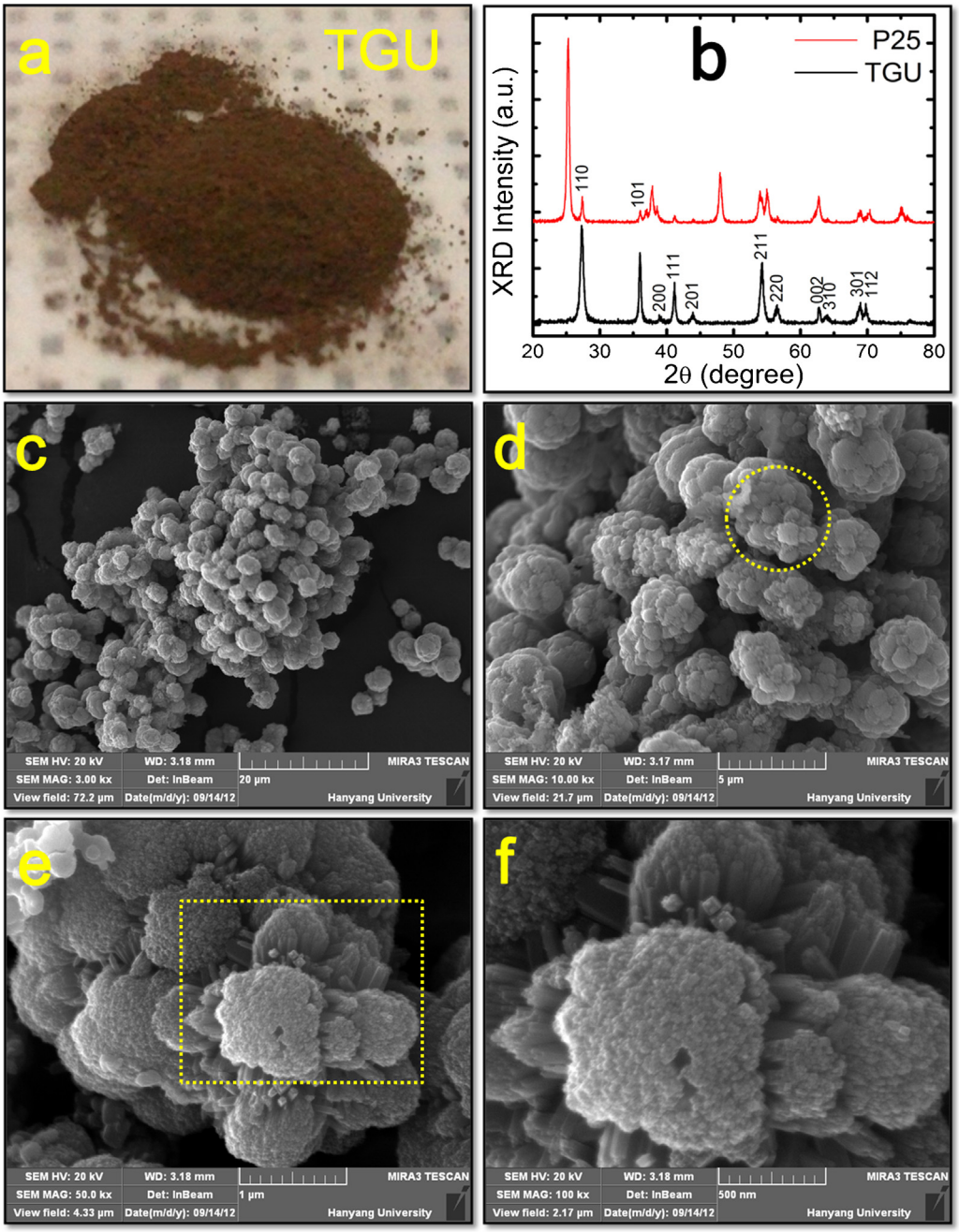

Fig. 1. (a, b) Physical appearance and XRD pattern of TGU. XRD pattern of P25 TiO_2 is also shown for a comparison. (c–f) FE-SEM images of the hydrothermally synthesized microspheres with stacked nanorods (TGU sample), depicting cauliflower like shape. The encircled area in (d) is magnified in (e) and the area marked in (e) is further magnified in (f) which shows the nanorods stacked in the form of microspheres.

pyrolysis-generated gases is comparatively high due to the thermal desorption of the adsorbed gases, which disrupts CN formation and perturbs its linkage with doped TiO_2. Single crystalline nature of TCN500 samples were confirmed from the spot diffraction pattern and HRTEM image (Fig. S3, Supplementary content).

3.3. Specific surface area, diffuse reflectance spectroscopy and energy band-gap analysis

N_2 adsorption–desorption isotherms obtained on the photocatalyst samples are shown in Fig. 4a and the data obtained is given in Table 1. TGU sample shows the lowest surface area, could be due to its large particle size (>2 μm). BET surface area of bare g-C_3N_4 from previous reports is found to be ~12 $m^2\,g^{-1}$ [42] and the surface area of TCN300 is almost of the sample value (10.67 $m^2\,g^{-1}$). The average pore diameter of the samples was analyzed from the Barrett–Joyner–Halenda (BJH) pore size distribution pattern shown in Fig. 4b. The data obtained (Table 1), is consistent with the

Table 1
Estimated values of energy band-gap (E_g), BET surface area and average pore diameter of the photocatalysts.

Sample	E_g (eV)	S_{BET} ($m^2\,g^{-1}$)	Average pore diameter (nm)
TGU	2.42	1.73	55.72
TCN300	2.66	10.67	9.16
TCN500	2.89	4.01	32.94
P25 TiO_2	3.16	54.03	17.14

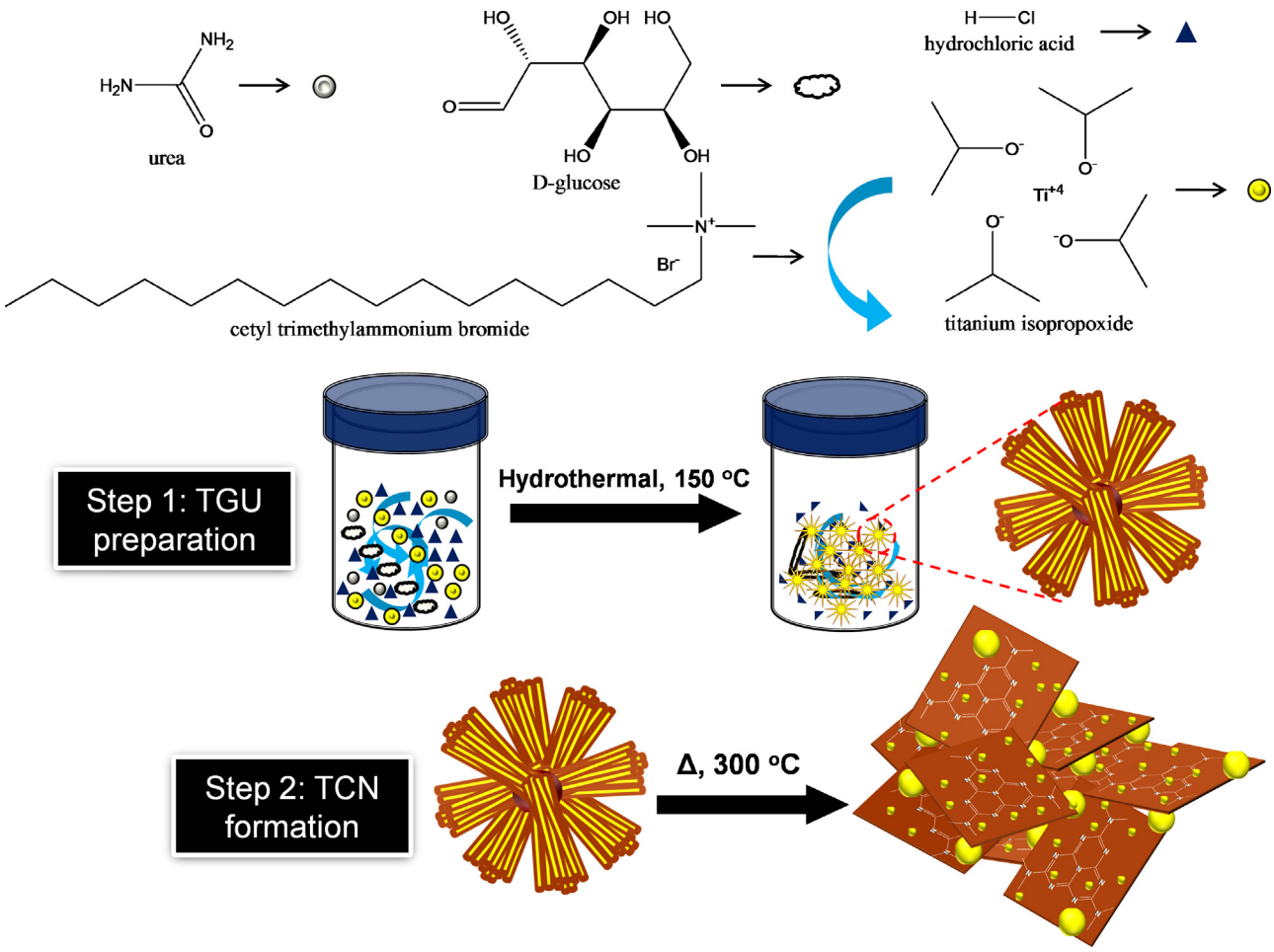

Scheme 1. Plausible growth mechanism depicting the growth of TGU microspherical nanorods and the formation of graphitic carbon nitride – TiO_2 composite (TCN). Top part shows the chemical structures of the reacting species.

size and morphology of the samples. It is well known that a sample with a large surface area does not necessarily guarantee enhanced photocatalytic activity. Isotherm and BJH pore size distribution plots for P25 TiO_2 is shown in Fig. S4 (Supplementary content).

The UV–vis diffuse reflectance spectra of all photocatalyst samples, including the reference P25 TiO_2 (Degussa) is shown in Fig. 5a. In comparison to P25, the absorption edges of the TGU samples are shifted toward the visible light region owing to the doping of C and N. The percentage of reflectance follows the order: TGU < TCN300 < TCN500 < P25 TiO_2 or in other words, TGU shows high visible light absorbance. This is obvious from the photographs depicting the color of the samples as shown in Figs. 1a–3a respectively, where the brown colored TGU sample can absorb more light in comparison to orange-tan colored TCN300 and yellow colored TCN500 respectively.

The energy band-gap from the UV–vis DRS spectra were calculated using the Kubelka–Munk theory. The Kubelka–Munk function for reflectance, $F(R)$ is given as,

$$F(R) = \frac{(1-R)^2}{2R} \tag{8}$$

where reflectance $R = R_{sample}/R_{reference}$ [55] Tauc plots are constructed using the Kubelka–Munk function for reflectance, $[F(R)\cdot h\nu]^{1/2}$ versus $h\nu$ from which the band gap energies were deduced by extrapolating the linear portion of Tauc's equation onto the energy axis as shown in Fig. 5b. The values of energy band-gaps of the photocatalysts are shown in Table 1. The energy band gap values follows the order P25 TiO_2 > TCN500 > TCN300 > TGU. TGU shows high absorbance capability with high C and N content, which is lost during its thermal treatment at high temperatures as has been discussed earlier. Thus, the band gap energy of TCN300 is lower than that of TCN500.

3.4. Visible light photocatalytic degradation of MB dye

UV–vis absorption spectra in Fig. 6a and b show the photocatalytic degradation of MB dye with respect to time, in the presence of TCN300 and TCN500 as the photocatalyst under visible light irradiation. Irradiating the reaction slurry with visible light ($\lambda > 400$ nm), results in a gradual and steady decrease of the absorbance peak formed at $\lambda_{max} = 665$ nm with respect to time. The percentage of dye degradation, η is calculated as

$$\eta = \frac{A_0 - A}{A_0} \times 100 \tag{9}$$

where A_0 is the initial absorbance of the dye and A is the time dependent absorbance. The plots showing the percentage of MB dye degradation with respect to time is presented in Fig. 6c. For a better comparison, the plots of MB dye degradation without photocatalyst and using P25 TiO_2 are also included. P25 TiO_2 could degrade less than 50% of the dye after 100 min of visible light irradiation because of its poor visible light absorption capability, owing to its large band gap (3.16 eV). At the same time period, MB dye degradation using TGU, TCN300 and TCN500 were ~98, ~93 and

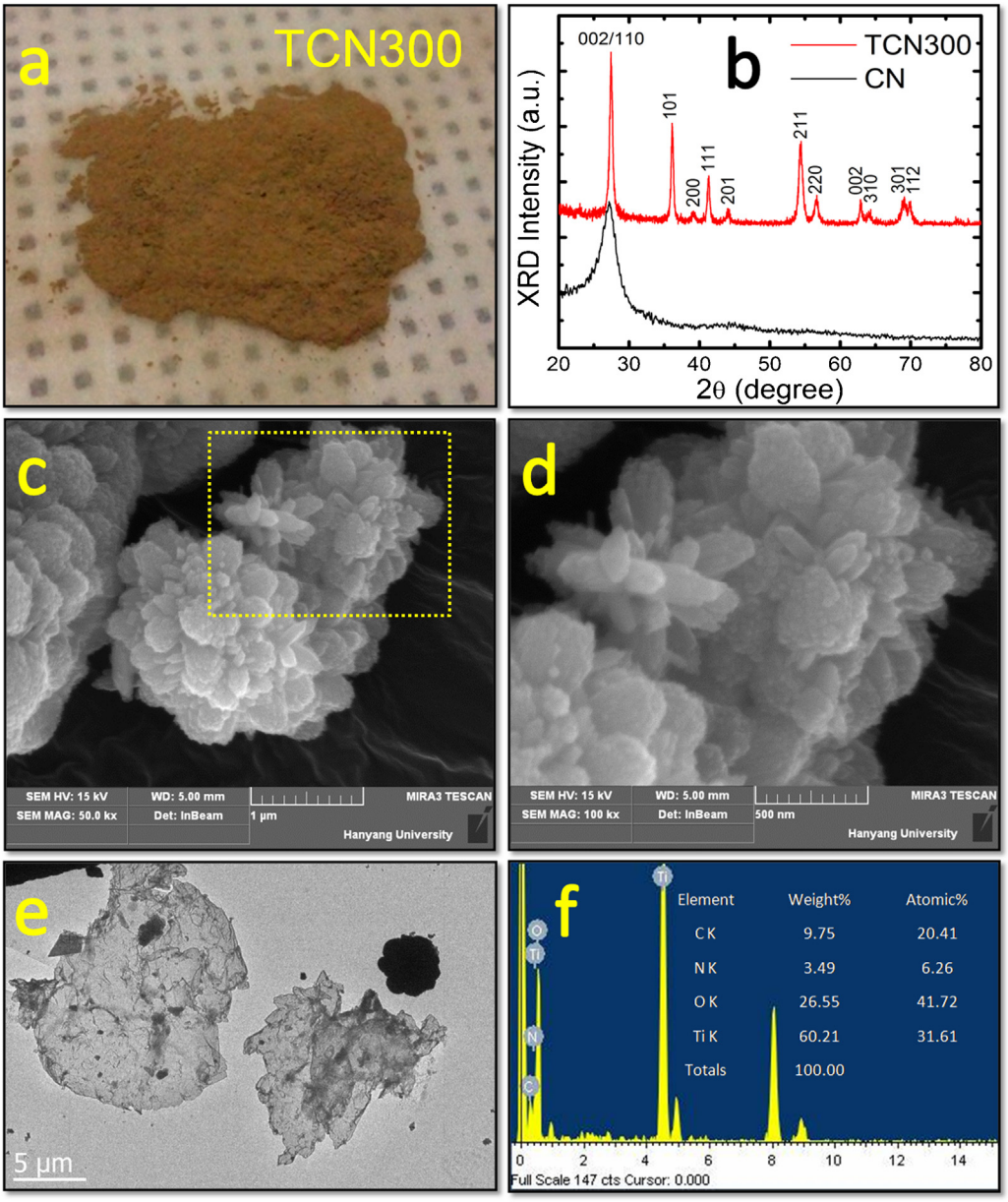

Fig. 2. (a, b) Color photograph of TCN300 photocatalyst and its XRD pattern. The XRD pattern of CN nanosheets obtained by etching TCN300 in HF is also shown. (c, d) FE-SEM images of TCN300 composite photocatalyst, the area marked in (c) is magnified in (d). (e) TEM image showing the doped TiO_2 particles intercalated between graphitic C_3N_4 nanosheets and (f) EDS spectra and its corresponding elemental composition is presented in the inset. (For interpretation of the references to color in this figure legend, the reader is referred to the web version of this article.)

~75%, respectively. Though TGU has high visible light absorption capability with a lower energy band gap in comparison to TCN300 and TCN500, the synergy developed between CN nanosheets and doped TiO_2 particles (during TCN formation) enhances the efficiency of MB dye degradation under visible light, which is discussed in detail in Section 3.5. Also, the large surface area of TCN composites (Table 1), in comparison to TGU could be a reason for the enhancement in the photocatalytic activity. Moreover, it could also be speculated that the presence of micron sized TiO_2 particles in TCN composites (Fig. 2) may enhance the light harvesting efficiency with multiple scattering effect as were applied for dye sensitized solar cells (DSSCs) [56,57]. The larger particle size, poor formation of CN and larger bandgap energy are the factors responsible for the reduction in the photocatalytic efficiency of TCN500, in comparison to TCN300. However, the presence of doped TiO_2 in TCN500, contributes to its intermediate photodegradation efficiency.

3.5. Electron transfer mechanism for MB dye photodegradation

It is well known that dye molecules absorb visible light, get excited and inject charge into the photocatalyst and assist during its photodegradation [58]. This is confirmed with the help of P25 TiO_2 nanoparticles as almost 50% of MB dye degraded by irradiating visible light for a period of 180 min (Fig. 6c). Scheme 2 shows the schematic of the electron transfer mechanism for the degradation of MB dye using TCN photocatalyst under visible light irradiation. CN is formed by the sp^2 hybridization between carbon and nitrogen, which depicts the π-conjugated graphitic planes and represents a structure similar to graphene [59]. Strong covalent bonding is reported to be the cause of the synergy between TiO_2 and other nanostructures of carbon such as graphene [54] and carbon nanotubes [60]. Thus, strong covalent bonding can be speculated as the reason for the synergy in TCN composites too. A synergistic

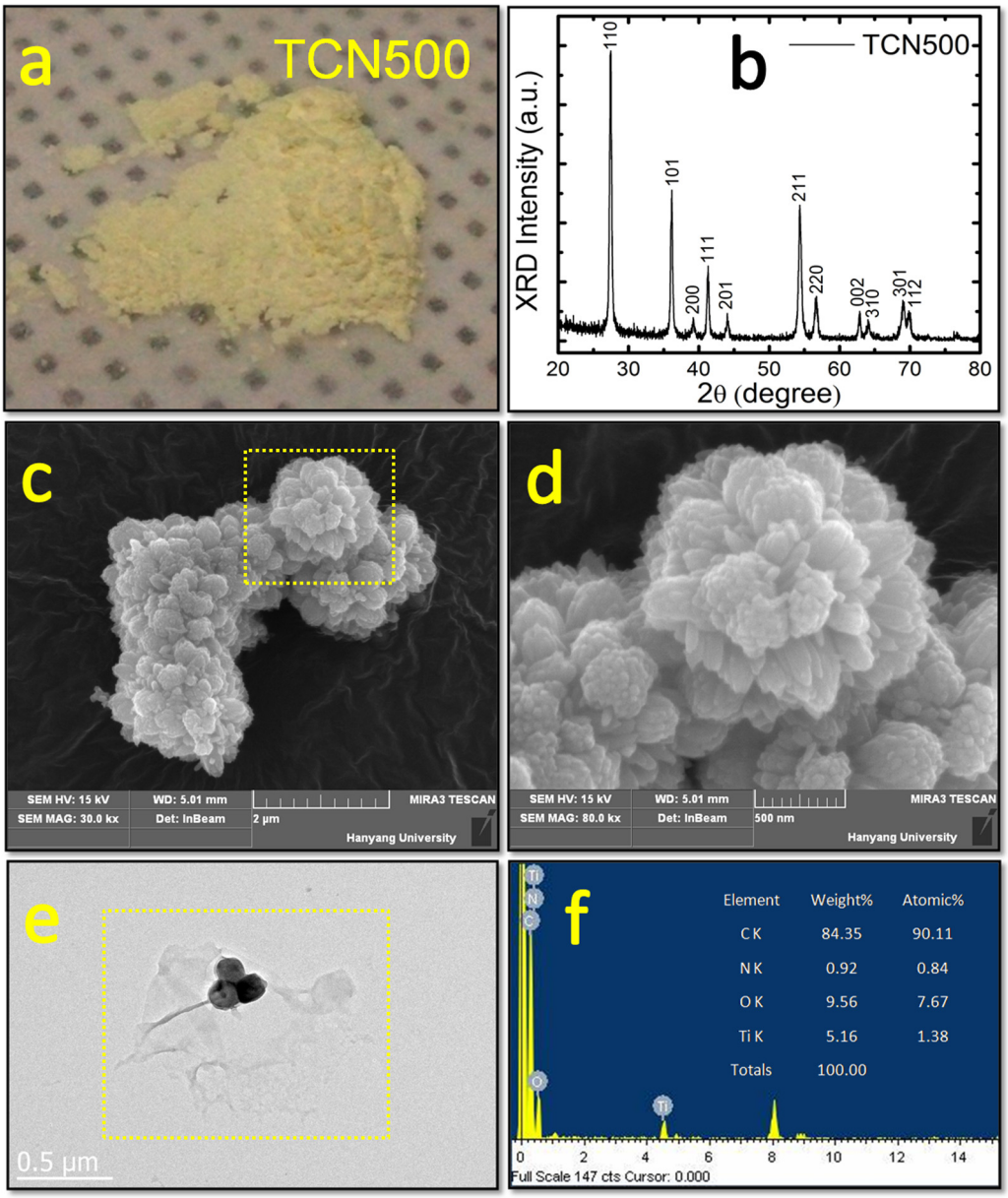

Fig. 3. (a, b) Color photograph and XRD pattern of TCN500 photocatalyst. FE-SEM images of TCN500 composite photocatalyst, the area marked in (c) is magnified in (d). (e) TEM image showing the as formed TCN500 composite. (f) EDS spectra obtained by scanning the area marked in c, the inset shows the corresponding elemental composition. (For interpretation of the references to color in this figure legend, the reader is referred to the web version of this article.)

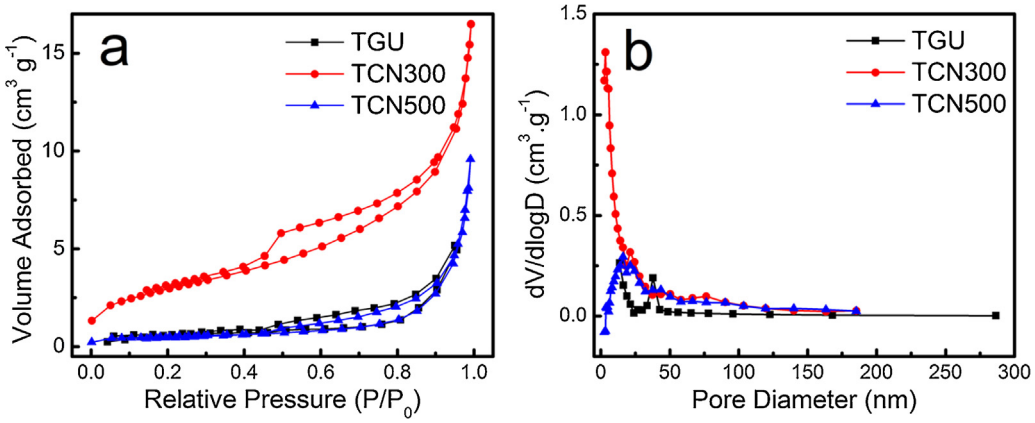

Fig. 4. (a) N_2 adsorption desorption isotherms measured at 77 K and (b) corresponding Barrett–Joyner–Halenda (BJH) pore-size distribution plots of photocatalyst samples.

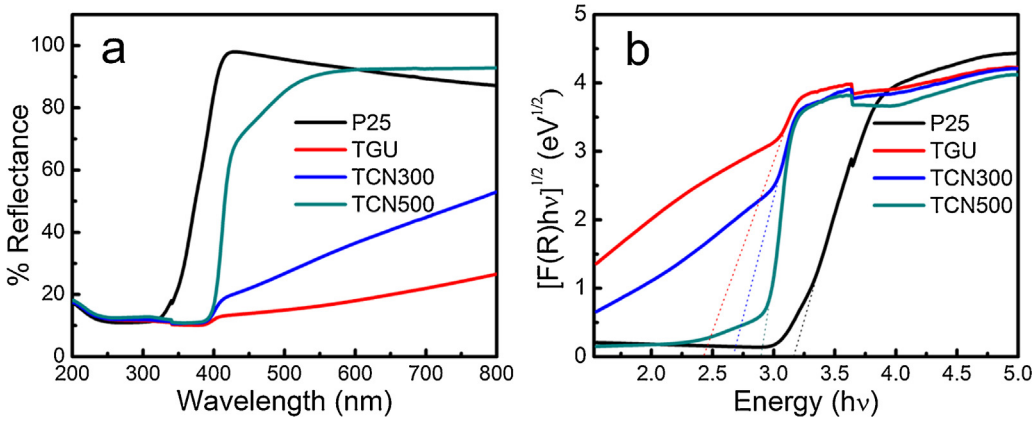

Fig. 5. (a) UV–vis diffuse reflectance spectra of the photocatalysts and (b) their corresponding Tauc's plots.

heterojunction is formed, at the interface between CN and doped TiO_2 (Scheme 2), and the enhanced photocatalytic activity because of its formation in TCN could be explained as follows:

(i) Charge formation: the ability of both CN and doped TiO_2, to absorb visible light, is the first advantage of the TCN composite system. When the system is irradiated with visible light, the e^- (electrons) get promoted from the VB to CB, either in doped TiO_2, or in CN, respectively and this creates h^+ (holes) [41]. The heterojunction system (Scheme 2), allows the photogenerated e^- in CN to easily enter the CB level of doped TiO_2. Similarly, the h^+ could easily migrate to the surface of CN [39]. The photogenerated electrons and holes are effectively collected by doped TiO_2 and CN, respectively.

(ii) Charge separation: synergistic heterojunction formation between CN and doped TiO_2, helps in the efficient $e^- - h^+$ separation (evidenced using PL spectroscopy). The interparticle charge transfer is promoted at the interface between CN and doped TiO_2. Similar interface presence has been reported to be cause for the enhanced photocatalytic activity in other CN composite heterojunction systems [42]. Also, doped rutile TiO_2 can possibly act as an electron sink in the TCN composite system to further reduce the $e^- - h^+$ pair recombination. Li et al. [42], prepared CN/$SmVO_4$ composites by the calcination of mixed powders of $SmVO_4$ and CN. However, they noticed poor photocatalytic activity at high temperature of calcination, which reduced the CN content. Thus the reduced photocatalytic activity of TCN500 could be attributed to the same reasons

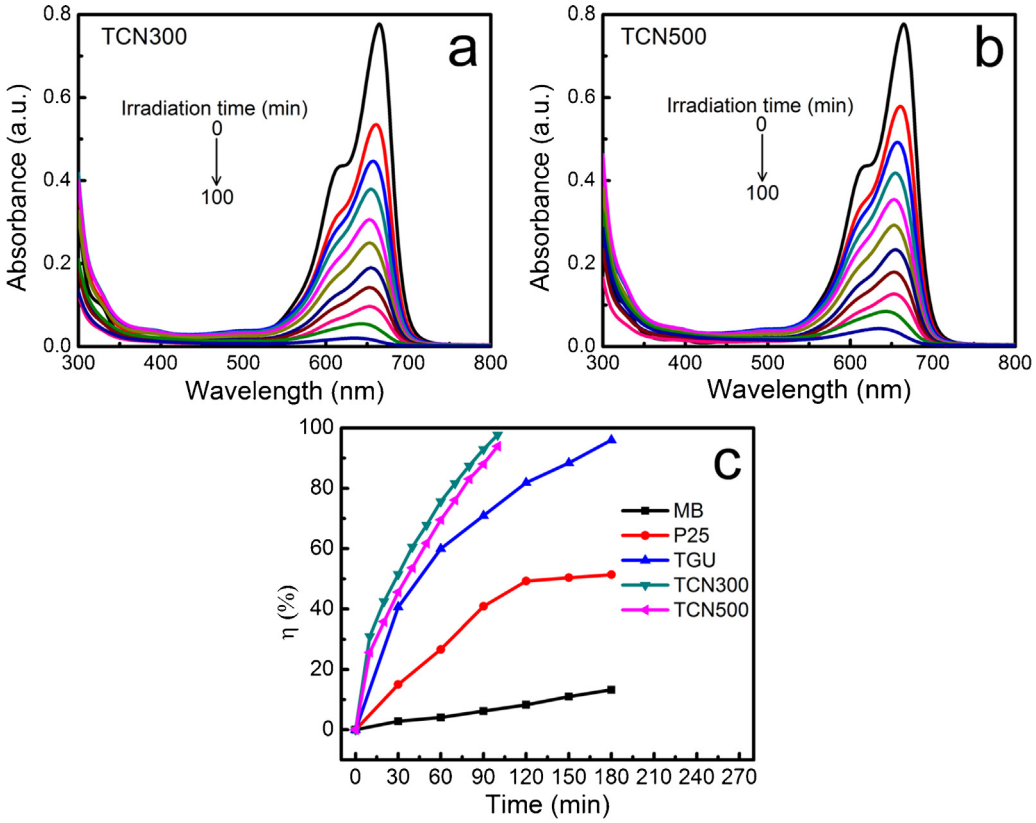

Fig. 6. (a, b) UV–vis absorption spectra showing the spectral degradation of MB dye in the presence of TCN300 and TCN500. (c) Plot showing the time dependent photodegradation of MB dye under visible light irradiation.

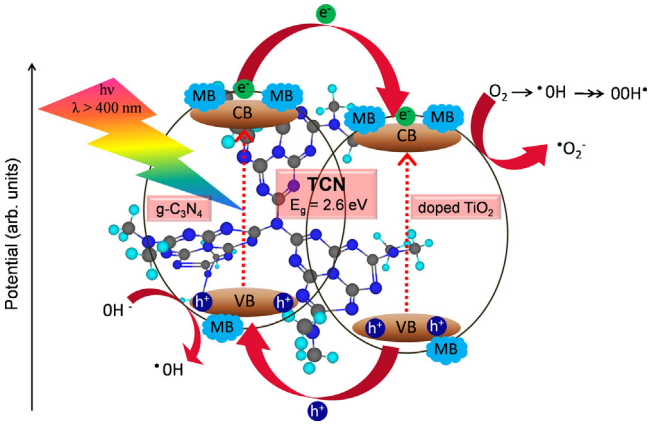

Scheme 2. Schematic representing the charge transfer for the photocatalytic degradation of MB dye under visible light in a synergistic composite system containing g-C_3N_4 and doped TiO_2 (TCN).

rendering in a poor interface contact between CN and doped TiO_2. The following reactions are predicted to take place during the visible light assisted photodegradation of MB dye using TCN composite.

$$\mathrm{TCN(g\text{-}C_3N_4 : \Pi^*)} \xrightarrow{h\nu(\lambda>400\,\mathrm{nm})} h^+ + e^- \quad (10)$$

$$\mathrm{TCN(doped\text{-}TiO_2)} \xrightarrow{h\nu(\lambda>400\,\mathrm{nm})} h_{VB}^+ + e_{CB}^- \quad (11)$$

$$\mathrm{MB_{ads} + TCN(}h^+\mathrm{)} \rightarrow \mathrm{MB_{ads}}* + \mathrm{TCN} \quad (12)$$

$$\mathrm{MB_{ads} + O_2(O_2{}^{-\bullet}, H_2O_2)} \rightarrow \text{degraded products} \quad (13)$$

The photodegradation of MB can be induced by (i) the electrons photo-excited to π^* and (ii) valance band holes of doped TiO_2 (h_{VB}^+). As depicted in Scheme 2, when TCN composite is irradiated with visible light, the above reactions (Eqs. (10) and (11)) lead to MB dye degradation. Electrons are scavenged by the molecular oxygen present in water to generate superoxide $O_2{}^{-\bullet}$ and hydrogen peroxide radical $^{\bullet}OOH$ (Eq. (13)). Holes (h^+) generated in the π orbital of CN and in the valance band of doped-TiO_2, readily react with the water molecules to produce hydroxyl radicals and eventually MB dye is degraded. Ge et al. [39] reported the degradation of methyl orange dye using g-C_3N_4/Bi_2WO_6 composites and it can be noted that TCN follows similar steps during the degradation of MB dye.

In order to investigate the influence of doping and the synergy of doped TiO_2 with CN nanosheets on the photocatalytic activity, photoluminescence (PL) spectroscopy studies were performed, through which the photogenerated recombination of $e^- - h^+$ pairs on each sample could be found out. Fig. 7 shows the PL spectra of the photocatalysts. The samples were excited at 230 nm and the emission spectra were recorded in a range between 300 and 600 nm. The high intensity emission peaks of P25 TiO_2 have broad peaks extending in between 400 and 500 nm corresponding to its mixed (rutile and anatase) phases. Compared to P25, the emission intensity is much lower for TCN and TGU samples, which suggest that their $e^- - h^+$ pair recombination rate is also much lower. Weak PL signal from TGU could be due to the presence of residues in the form of isocyanic acid and hydroxyl ions, which suppress the generation of $e^- - h^+$ pair. Also many studies have proven that the emission intensity is inversely proportional to particle size [61,62] and thus it could be speculated that TGU sample with larger particle size shows much lower emission intensity than TCN composites. On the other hand, the presence of a synergistic heterojunction in TCN composites enhances the generation of $e^- - h^+$ pairs, is confirmed

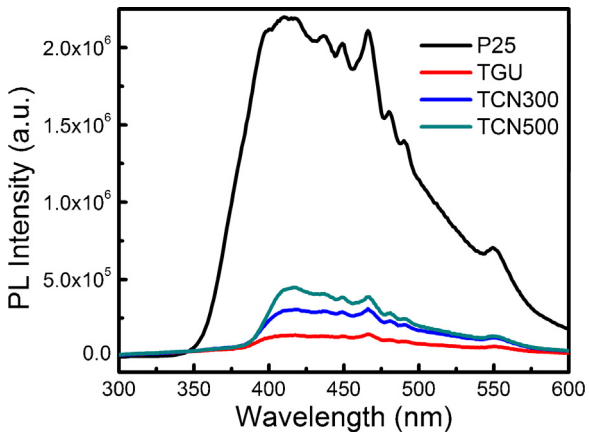

Fig. 7. Photoluminescence spectra of the photocatalysts.

with the increase in their PL emission intensity. The better linkage of doped TiO_2 with CN nanosheets in TCN300 leads to a better electron transfer and decreases the PL emission intensity, compared to TCN500. Similar increase in PL emission intensity was reported by Zhou et al. [54], for TiO_2–graphene composite system, when the linkage/bonding between TiO_2 and graphene was poor.

3.6. Photocatalytic reduction of Cr(VI)

Cr(VI) is a toxic and carcinogenic inorganic pollutant and hence it is alarmingly important to be removed from water. Many groups have reported the synergistic effect of simultaneous photodegradation of dye/organic molecules and reduction of heavy metal ions such as Cr(VI) in the presence of a photocatalyst under UV and visible light irradiation [63–66]. It was found that the synergistic effect complements each other and remarkably increased the removal rates [67]. Holes are produced rapidly in the presence of organic pollutants, suppresses the $e^- - h^+$ pair recombination and accelerates the reduction of Cr(VI) using photogenerated e^-. The emission studies reveal the enhanced charge separation in TCN photocatalyst and is feasible to be used in the photo-reduction of Cr(VI).

UV–vis absorption spectra in Fig. 8a and b show the visible light assisted photo-reduction of Cr(VI), in the presence of TCN300 and TCN500, respectively. Gradual and steady decrease in the intensity of the absorbance peak formed at λ_{max} = 364 nm with respect to time mark the photo-reduction of Cr(VI). The percentage of dye degradation, η is calculated using the formula given in Eq. (9). Plots showing the percentage of Cr(VI) reduction with respect to time is given in Fig. 8c. It is well known that alternation of pH of the reaction slurry improves the rate of removal of Cr(VI) and for which the mechanism [68,69] can be given by the following equations (Eqs. (14) and (15)).

$$(\mathrm{pH:\ Acidic})\ 2Cr_2O_7 + 16H^+ \rightarrow 4Cr^{3+} + 8H_2O + 3O_2 \quad (14)$$

$$(\mathrm{pH:\ Neutral\ or\ Alkaline})\ 4CrO_4{}^{2-} + 20H^+ \rightarrow 4Cr^{3+} + 10H_2O + 3O_2 \quad (15)$$

To test the efficiency of the photocatalyst, all the experiments for the photo reduction of Cr(VI) were carried out at its natural pH (~5, acidic) of the solution. The plots of the Cr(VI) reduction against irradiation time is presented in Fig. 8c. Approximately 72 and ~45% of Cr(VI) was photo-reduced using TCN300 and TCN500 after 100 min of visible light irradiation, respectively. TGU at the same time was able to reduce ~33% of Cr(VI). The synergistic heterojunction formation between CN nanosheets with doped TiO_2 is again expected

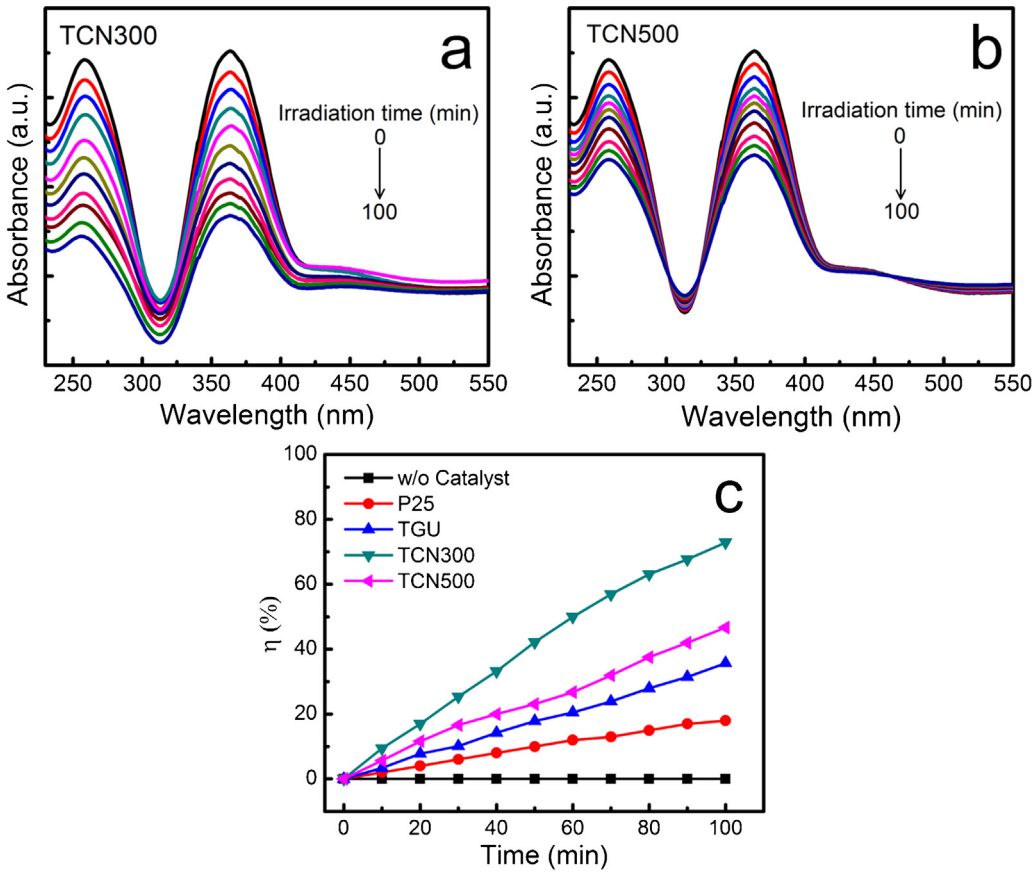

Fig. 8. (a, b) UV–vis absorption spectra showing the reduction of Cr(VI) ions in the presence of TCN300 and TCN500. (c) Plot showing the time dependent photo reduction of Cr(VI) ions under visible light irradiation in the presence of different catalysts.

to play an important role in the enhanced photo-reduction of Cr(VI) as were discussed previously in the case of MB dye degradation. Recently Qiu et al. [70] reported that poly(fluorene-co-thiophene) [PFT] could reduce Cr(VI) by itself and could also act as an electron donor/sensitizer when combined with TiO_2 for the photo-reduction of Cr(VI). PFT sensitizes TiO_2 and the electrons which move to the e^-_{CB} are captured by the Cr(VI) ions, results in their reduction in the form of a less toxic Cr(III). But their system eventually was believed to fail owing to the lack of electron donors to refill the holes in the HOMO of PFT. In our case, since both CN nanosheets and doped TiO_2 can absorb visible light, the aforementioned problem can be ruled out and thus the TCN photocatalytic system is believed to work efficiently.

4. Conclusion

In conclusion, we demonstrated a novel method for the preparation of graphitic carbon nitride TiO_2 (g-C_3N_4–TiO_2) composite photocatalyst, by a thermal transformation approach. C and N co-doped Titanium oxide (TGU) nanorods, stacked in the form of microspheres were prepared hydrothermally. Urea, the N source, under hydrothermal conditions, acts as the base catalyst for the formation of nanorods and D-glucose, was employed as an additional carbon source. The presence of cetyltrimethylammonium bromide, stacks the nanorods in the form of microspheres, was confirmed using SEM. Thermal treatment of the hydrothermally synthesized TGU sample in open air at 300 °C resulted in the synergistic formation of g-C_3N_4–TiO_2 (TCN) composite, were confirmed using TEM and EDS spectroscopy. Similar thermal treatment at a higher temperature (500 °C), suppressed the formation of g-C_3N_4 and perturbed its linkage with doped TiO_2. The detailed growth mechanisms for the formation of microspherical nanorods and its transformation to TCN were discussed. Pyrolysis generated g-C_3N_4 is bound to doped TiO_2, by strong covalent bonding, which induces a synergy between their interface. Thus, the heterojunction formed between g-C_3N_4 and doped TiO_2 was named as "synergistic heterojunction". Visible light photocatalytic efficiency of the prepared photocatalysts were investigated by monitoring the degradation of Methylene Blue (MB) dye and the reduction of Cr(VI) ions. Key factors responsible for the enhancement in the photocatalytic efficiency of TCN composites (TCN300) were, (i) the synergy formed between g-C_3N_4 nanosheets and doped TiO_2, enhances electron transport and electron–hole pair separation and (ii) the combined ability of both g-C_3N_4 and doped TiO_2 to absorb visible light. Electron transfer mechanisms in the synergistic heterojunction, such as the charge formation and separation were discussed using the band diagram. The influence of synergistic heterojunction on the enhanced photocatalytic efficiency, were investigated using PL spectroscopy. TCN composites could prove to be an ideal material for applications in visible light induced hydrogen energy production and also could show enhanced photo reduction ability.

Acknowledgements

This work was supported by the National Research Foundation of Korea (NRF) grant funded by the Korea government (MEST) (No. 2012R1A2A2A01047579), and the Human Resources Development program (No. 20124030200130) of the Korea Institute of Energy

Technology Evaluation and Planning (KETEP) grant funded by the Korea government Ministry of Trade, Industry and Energy.

Appendix A. Supplementary data

Supplementary data associated with this article can be found, in the online version, at http://dx.doi.org/10.1016/j.apcatb.2013.05.077.

References

[1] N. Semagina, L. Kiwi-Minsker, Catalysis Reviews 51 (2009) 147–217.
[2] F.S. Kim, G. Ren, S.A. Jenekhe, Chemistry of Materials 23 (2010) 682–732.
[3] A. Vaneski, A.S. Susha, J. Rodríguez-Fernández, M. Berr, F. Jäckel, J. Feldmann, A.L. Rogach, Advanced Functional Materials 21 (2011) 1547–1556.
[4] V. Tamilselvan, S. Kishore, K.N. Rao, P. Reji, Journal of Physics D: Applied Physics 43 (2010) 385402.
[5] K. Sridharan, V. Tamilselvan, D. Yuvaraj, K. Narasimha Rao, R. Philip, Optical Materials 34 (2012) 639–645.
[6] R. Agarwal, C.M. Lieber, Applied Physics A 85 (2006) 209–215.
[7] I. Paramasivam, H. Jha, N. Liu, P. Schmuki, Small 8 (2012) 3073–3103.
[8] M. Ni, M.K.H. Leung, D.Y.C. Leung, K. Sumathy, Renewable & Sustainable Energy Reviews 11 (2007) 401–425.
[9] H. Choi, P.K. Santra, P.V. Kamat, ACS Nano 6 (2012) 5718–5726.
[10] K. Sivaranjani, S. Agarkar, S.B. Ogale, C.S. Gopinath, Journal of Physical Chemistry C 116 (2012) 2581–2587.
[11] W.J. Youngblood, S.H.A. Lee, K. Maeda, T.E. Mallouk, Accounts of Chemical Research 42 (2009) 1966–1973.
[12] K. Maeda, K. Domen, Journal of Physical Chemistry Letters 1 (2010) 2655–2661.
[13] K. Mori, H. Yamashita, M. Anpo, RSC Advances 2 (2012) 3165–3172.
[14] K. Sridharan, T.J. Park, Applied Catalysis B: Environmental 134–135 (2013) 174–184.
[15] M. Pelaez, N.T. Nolan, S.C. Pillai, M.K. Seery, P. Falaras, A.G. Kontos, P.S.M. Dunlop, J.W.J. Hamilton, J.A. Byrne, K. O'Shea, M.H. Entezari, D.D. Dionysiou, Applied Catalysis B-Environmental 125 (2012) 331–349.
[16] X. Chen, S.S. Mao, Chemical Reviews 107 (2007) 2891–2959.
[17] G. Liu, L.Z. Wang, H.G. Yang, H.M. Cheng, G.Q. Lu, Journal of Materials Chemistry 20 (2010) 831–843.
[18] S. Rehman, R. Ullah, A.M. Butt, N.D. Gohar, Journal of Hazardous Materials 170 (2009) 560–569.
[19] A. Kubacka, M. Fernandez-Garcia, G. Colon, Chemical Reviews 112 (2012) 1555–1614.
[20] R. Leary, A. Westwood, Carbon 49 (2011) 741–772.
[21] S. Bingham, W.A. Daoud, Journal of Materials Chemistry 21 (2011) 2041–2050.
[22] J.V. Badding, Advanced Materials 9 (1997) 877–886.
[23] A. Thomas, A. Fischer, F. Goettmann, M. Antonietti, J.O. Muller, R. Schlogl, J.M. Carlsson, Journal of Materials Chemistry 18 (2008) 4893–4908.
[24] F. Goettmann, A. Fischer, M. Antonietti, A. Thomas, Angewandte Chemie-International Edition 45 (2006) 4467–4471.
[25] F. Goettmann, A. Thomas, M. Antonietti, Angewandte Chemie-International Edition 46 (2007) 2717–2720.
[26] F. Goettmann, A. Fischer, M. Antonietti, A. Thomas, New Journal of Chemistry 31 (2007) 1455–1460.
[27] S.J. Yang, J.H. Cho, G.H. Oh, K.S. Nahm, C.R. Park, Carbon 47 (2009) 1585–1591.
[28] X.C. Wang, K. Maeda, A. Thomas, K. Takanabe, G. Xin, J.M. Carlsson, K. Domen, M. Antonietti, Nature Materials 8 (2009) 76–80.
[29] X.X. Zou, G.D. Li, Y.N. Wang, J. Zhao, C. Yan, M.Y. Guo, L. Li, J.S. Chen, Chemical Communications 47 (2011) 1066–1068.
[30] J.H. Liu, T.K. Zhang, Z.C. Wang, G. Dawson, W. Chen, Journal of Materials Chemistry 21 (2011) 14398–14401.
[31] Y. Di, X.C. Wang, A. Thomas, M. Antonietti, Chemcatchem 2 (2010) 834–838.
[32] L. Ge, C.C. Han, J. Liu, Y.F. Li, Applied Catalysis A-General 409 (2011) 215–222.
[33] X.F. Chen, J.S. Zhang, X.Z. Fu, M. Antonietti, X.C. Wang, Journal of the American Chemical Society 131 (2009) 11658–11659.
[34] Y.J. Zhang, T. Mori, J.H. Ye, M. Antonietti, Journal of the American Chemical Society 132 (2010) 6294–6295.
[35] S.C. Yan, Z.S. Li, Z.G. Zou, Langmuir 26 (2010) 3894–3901.
[36] G. Liu, P. Niu, C.H. Sun, S.C. Smith, Z.G. Chen, G.Q. Lu, H.M. Cheng, Journal of the American Chemical Society 132 (2010) 11642–11648.
[37] L. Ge, C.C. Han, Applied Catalysis B-Environmental 117 (2012) 268–274.
[38] Q.J. Xiang, J.G. Yu, M. Jaroniec, Journal of Physical Chemistry C 115 (2011) 7355–7363.
[39] L. Ge, C.C. Han, J. Liu, Applied Catalysis B-Environmental 108 (2011) 100–107.
[40] S.C. Yan, S.B. Lv, Z.S. Li, Z.G. Zou, Dalton Transactions 39 (2010) 1488–1491.
[41] H. Xu, J. Yan, Y. Xu, Y. Song, H. Li, J. Xia, C. Huang, H. Wan, Applied Catalysis B: Environmental 129 (2013) 182–193.
[42] T. Li, L. Zhao, Y. He, J. Cai, M. Luo, J. Lin, Applied Catalysis B: Environmental 129 (2013) 255–263.
[43] X. Zhou, B. Jin, R. Chen, F. Peng, Y. Fang, Materials Research Bulletin 48 (2013) 1447–1452.
[44] H.J. Yan, H.X. Yang, Journal of Alloys and Compounds 509 (2011) L26–L29.
[45] J.G. Yu, H.G. Yu, B. Cheng, M.H. Zhou, X.J. Zhao, Journal of Molecular Catalysis a-Chemical 253 (2006) 112–118.
[46] L. Liu, Y.P. Zhao, H.J. Liu, H.Z. Kou, Y.Q. Wang, Nanotechnology 17 (2006) 5046–5050.
[47] S.W. Liu, J.G. Yu, S. Mann, Nanotechnology 20 (2009).
[48] J.G. Yu, S.W. Liu, H.G. Yu, Journal of Catalysis 249 (2007) 59–66.
[49] F. Dong, H.Q. Wang, Z.B. Wu, Journal of Physical Chemistry C 113 (2009) 16717–16723.
[50] X.L. Hu, J.C. Yu, J.M. Gong, Journal of Physical Chemistry C 111 (2007) 5830–5834.
[51] M.M. Titirici, M. Antonietti, A. Thomas, Chemistry of Materials 18 (2006) 3808–3812.
[52] M.M. Titirici, M. Antonietti, N. Baccile, Green Chemistry 10 (2008) 1204–1212.
[53] D. Mitoraj, H. Kisch, Angewandte Chemie-International Edition 47 (2008) 9975–9978.
[54] K. Zhou, Y. Zhu, X. Yang, X. Jiang, C. Li, New Journal of Chemistry 35 (2011) 353–359.
[55] C. Han, M. Pelaez, V. Likodimos, A.G. Kontos, P. Falaras, K. O'Shea, D.D. Dionysiou, Applied Catalysis B-Environmental 107 (2011) 77–87.
[56] J. Ferber, J. Luther, Solar Energy Materials and Solar Cells 54 (1998) 265–275.
[57] S. Hore, P. Nitz, C. Vetter, C. Prahl, M. Niggemann, R. Kern, Chemical Communications (2005) 2011–2013.
[58] M. Mrowetz, W. Balcerski, A.J. Colussi, M.R. Hoffmann, Journal of Physical Chemistry B 108 (2004) 17269–17273.
[59] X.C. Wang, X.F. Chen, A. Thomas, X.Z. Fu, M. Antonietti, Advanced Materials 21 (2009) 1609–1612.
[60] S.K. Yadav, S.R. Madeshwaran, J.W. Cho, Journal of Colloid and Interface Science 358 (2011) 471–476.
[61] A. van Dijken, E.A. Meulenkamp, D. Vanmaekelbergh, A. Meijerink, Journal of Physical Chemistry B 104 (2000) 1715–1723.
[62] P.K. Sharma, M.H. Jilavi, R. Nass, H. Schmidt, Journal of Luminescence 82 (1999) 187–193.
[63] S.G. Schrank, H.J. Jose, R. Moreira, Journal of Photochemistry and Photobiology A-Chemistry 147 (2002) 71–76.
[64] L.M. Wang, N. Wang, L.H. Zhu, H.W. Yu, H.Q. Tang, Journal of Hazardous Materials 152 (2008) 93–99.
[65] C.R. Chenthamarakshan, K. Rajeshwar, E.J. Wolfrum, Langmuir 16 (2000) 2715–2721.
[66] N. Wang, L.H. Zhu, Y.P. Huang, Y.B. She, Y.M. Yu, H.Q. Tang, Journal of Catalysis 266 (2009) 199–206.
[67] H. Kyung, J. Lee, W.Y. Choi, Environmental Science & Technology 39 (2005) 2376–2382.
[68] M.I. Litter, Applied Catalysis B-Environmental 23 (1999) 89–114.
[69] R. Vinu, G. Madras, Environmental Science & Technology 42 (2008) 913–919.
[70] R.L. Qiu, D.D. Zhang, Z.H. Diao, X.F. Huang, C. He, J.L. Morel, Y. Xiong, Water Research 46 (2012) 2299–2306.